Formation and steady-state maintenance of field reversed configuration using rotating magnetic field current drive

H. Y. Guo, A. L. Hoffman, R. D. Brooks, A. M. Peter, Z. A. Pietrzyk, S. J. Tobin,[a] and G. R. Votroubek
Redmond Plasma Physics Laboratory, University of Washington, Seattle, Washington 98195

(Received 11 July 2001; accepted 15 October 2001)

Rotating magnetic fields (RMF) have been used to both form and maintain field reversed configurations (FRC) in quasisteady state. These experiments differ from steady-state rotamaks in that the FRCs are similar to those formed in theta-pinch devices, that is elongated and confined inside a flux conserver. The RMF creates an FRC by driving an azimuthal current which reverses an initial positive bias field. The FRC then expands radially, compressing the initial axial bias flux and raising the plasma density, until a balance is reached between the RMF drive force and the electron–ion friction. This generally results in a very high ratio of separatrix to flux conserver radius. The achievable final conditions are compared with simple analytic models to estimate the effective plasma resistivity. The RMF torque on the electrons is quickly transferred to the ions, but ion spin-up is limited in these low density experiments, presumably by ion-neutral friction, and does not influence the basic current drive process. However, the ion rotation can result in a rotating $n=2$ distortion if the separatrix radius is too far removed from the plasma tube wall. © *2002 American Institute of Physics.* [DOI: 10.1063/1.1426102]

I. INTRODUCTION

Field reversed configuration (FRC) formation and steady-state maintenance with Rotating magnetic fields (RMF) has been demonstrated in a series of rotamak experiments, but those facilities had no flux conserver and, if the RMF force was strong enough to overcome electron–ion friction, the FRC simply expanded until it contacted the plasma tube wall.[1–3] This resulted in relatively cold plasmas ($T_e \sim 10-20$ eV) with much of the plasma pressure supported by the wall. The plasmas formed in those devices were also near spherical, and many of the one-dimensional descriptions developed for elongated FRCs confined in cylindrical flux conservers are not applicable. A new device, the Translation, Confinement, and Sustainment (TCS) experiment,[4] was constructed at the Redmond Plasma Physics Laboratory (RPPL) to study the sustainment and flux build-up of hot FRCs formed by the normal theta-pinch technique, and then translated and expanded into a chamber with RMF drive coils. However, this device has only been used, so far, to study the formation of FRCs using RMF alone. Due to the high power required to overcome initial radiation barriers and form hot, high beta plasmas, large FRCs formed by RMF alone will generally be limited to low temperatures. Thus, the TCS formed FRCs have electron temperatures in the 20–60 eV range. This is similar to the temperature range of FRCs formed in the smaller Star Thrust Experiment (STX) device at RPPL, but those FRCs could not be sustained for reasons that are not completely understood.[5,6]

When an RMF is applied to a preionized gas inside a flux conserver, with a given bias field, an azimuthal current will be generated if the force on the electrons exceeds the electron–ion friction. This condition has been represented in the literature as requiring that the magnetization parameter $\gamma = \omega_{ce}/\nu_{ei}$ exceeds the penetration parameter $\lambda = r_s/\delta$. Here $\omega_{ce} = eB_\omega/m_e$ is the electron cyclotron frequency in the RMF field B_ω, and ν_{ei} is the electron ion collision frequency. r_s is the plasma or separatrix radius and $\delta = (2\eta/\mu_0\omega)^{1/2}$ is the normal penetration skin depth of an RMF with frequency ω into a plasma column with resistivity $\eta = m_e\nu_{ei}/n_e e^2$. In this notation δ would depend on the parallel collision frequency or resistivity and γ on $(\nu_\parallel \nu_\perp)^{1/2}$. It is only the ratio of γ/λ, that is important, so it is the cross field resistivity or collisionality that governs the force balance.[7] The plasma currents that can be driven will then depend on both the cross-field resistivity and the electron density since, for a specified resistivity (which is used in modeling), a lower electron density implies a lower collisionality, and thus better magnetization and force balance.

Simple analytic expressions have been derived for the force on the electrons exerted by the RMF.[7] These are used with the measured electron density and plasma current to determine the effective cross-field resistivity. The final attainable confinement field will then depend on the value of anomalous resistivity and the plasma temperature, inasmuch as temperature and density are inversely related in a high beta plasma such as the FRC. In the present experiments at $\sim 10^{19}$ m^{-3} densities the plasma temperature is limited by ionization, convection, and radiation losses since there appears to be a large neutral fraction, at least in the current carrying edge region. The inferred value of cross-field resistivity is also high [higher even than the empirical scaling given by the Large s Experiment (LSX)[8]], which may be due

[a]Also at Los Alamos National Laboratory, MS-E526, Los Alamos, New Mexico.

to a low ion temperature and a high ratio of electron drift speed to ion thermal velocity, a relatively lower magnetic field, or simply to the particular drive process encountered in these experiments. A large RMF torque is required to overcome this high resistivity. The ions should rapidly spin-up close to the RMF frequency if they were not retarded by other means. This is not observed, with the ion rotational speed never becoming greater than 0.2ω. It is assumed that the neutrals provide this breaking action as has been calculated by several authors.[9,10]

The simple analytic scaling, further refined using one-dimensional MHD codes,[11] is outlined in Sec. II. TCS was originally run at an RMF frequency of 180 kHz ($\omega = 10^6$ rad/s), and results from these experiments, along with a brief description of the experimental geometry, are given in Sec. III. The requirements to produce steady state operation are discussed there. It was found that the electron density produced under those conditions, although low, was high enough relative to the achievable confinement field, that the ratio of actual line current needed to reverse the external field to the line current that would be produced by full synchronous rotation of the electrons was low. This ratio of $I'_{\mathrm{rev}} = 2B_e/\mu_0$ to $I'_{\mathrm{sync}} = 0.5\langle n_e\rangle e\omega r_s^2$ is called ζ,

$$\zeta = \frac{I'_{\mathrm{rev}}}{I'_{\mathrm{sync}}} = \frac{4B_e}{\mu_0\langle n_e\rangle e\omega r_s^2}. \tag{1}$$

When ζ is low the current tends to be carried in a narrow region Δr near the separatrix. Assuming near synchronous electron rotation and a linear density profile in this region with maximum value n_{em}, the line current would be $\sim 0.5 n_{em} e\omega r_s \Delta r$. Since this current is one-half the total reversal current, one can write Δr in terms of ζ,

$$\Delta r = \frac{1}{2}\frac{\langle n_e\rangle}{n_{em}}\zeta r_s = \frac{1}{2}\langle\beta\rangle\zeta r_s, \tag{2}$$

where the latter equality holds if the temperature is uniform. It should be noted I'_{rev} is set by radial pressure equilibrium. The equilibrium driven line current cannot exceed this value. If the net RMF drive exceeded the net friction (expressed in Ref. 7 in terms of torques), the FRC would expand and raise B_e. [For an FRC confined in a flux conserver with fixed bias flux $\pi r_c^2 B_0$, where B_0 is the initial bias field and r_c is the flux conserver radius, the external field is set by $B_e = B_0/(1-x_s^2)$ with $x_s \equiv r_s/r_c$.] I'_{rev} will increase due to this increase in confinement field, but I'_{sync} will also tend to increase as the plasma is compressed to a higher density, and any change in ζ will be dependent on how the temperature changes. It is assumed in the simple analytical models that the FRC length can adjust arbitrarily to changes in radius and plasma density, but this will, of course, actually depend on plasma fueling and loss rates, and energy supply and loss.

Low ζ and low $\Delta r/r_s$ is undesirable since it increases the effective circuit resistance, $\sim 2\pi r_s \eta_\perp/\Delta r$, and makes the drive process less efficient. The RMF frequency ω was thus lowered to 0.5×10^6 rad/s to try and increase ζ. As expected, this has significantly increased ζ at a given density and allowed for operating at higher densities at similar ζ. The higher electron density appeared to limit the neutral penetration, and the ion spin-up frequency was higher than for the higher ω experiments, despite the lower drive frequency. This usually resulted in development of the standard $n=2$ rotational instability which, while not always disrupting the FRC, made data interpretation more difficult. Most data were thus taken with the FRC separatrix close to the plasma tube wall, which suppressed the $n=2$ distortion. These results are given in Sec. IV. Finally, a discussion of the implications of these results is given in Sec. V.

II. ANALYTIC SCALING

The analytic scaling used in analysis of the data presented in this paper is based on the model developed in Ref. 7. The RMF can penetrate into a plasma column if the drive force is sufficient to spin the electrons up to near synchronous rotation ω_r such that $\varpi = \omega - \omega_r$ is small. Then the effective penetration depth increases to $\delta^* = (2\eta/\mu_0\varpi)^{1/2}$. Simple penetration analysis of fixed density (no pressure adjustment) plasma columns showed that the $\gamma > \lambda$ condition was equivalent to having $\delta^* > r_s$.[12] Numerical calculations showed this process to be very nonlinear, with very little current being driven until γ equaled λ, and then full synchronous current driven when γ exceeded λ.[13,14]

The process is very different for a true FRC inside a flux conserver. Once the driven current is high enough to reverse the external field, the FRC will expand radially, increasing the density, and will reach an equilibrium condition where the drive and friction forces are in balance. The RMF will not penetrate beyond the FRC field null under this scenario. The RMF drive force is equal to $\langle j_z B_r\rangle$ where $j_z \sim (\varpi/\omega)E_z/\eta_\parallel$ is the axial current driven by the oscillating axial electric field $E_z = \omega r B_r$ produced by the RMF, reduced by the $j_\theta B_r$ Hall term, and B_r is the radial component of the RMF. Analytical solutions for j_z, B_r, and B_θ (which can be used to calculate an inward radial force) in the limit of partial penetration, were given in Ref. 7,

$$j_z = \left\{\exp\left(-i\left[\frac{\pi}{4} + \frac{a-r}{\delta^*}\right]\right)\right\} 2\sqrt{\frac{2a}{r}}\frac{B_\omega}{\mu_0\delta^*}e^{-[(a-r)/\delta^*]}, \tag{3}$$

$$B_r = \left\{\exp\left(-i\left[\frac{\pi}{4} + \frac{a-r}{\delta^*}\right]\right)\right\} \sqrt{\frac{2a}{r}}\frac{\delta^* B_\omega}{r}e^{-[(a-r)/\delta^*]}, \tag{4}$$

$$B_\theta = \left\{\exp\left(-i\left[\frac{\pi}{2} + \frac{a-r}{\delta^*}\right]\right)\right\} 2\sqrt{\frac{a}{r}}B_\omega e^{-[(a-r)/\delta^*]}. \tag{5}$$

The plasma column radius was a, which is approximately equal to r_s. The bracketed terms give the phase of the oscillating quantities relative to what j_z and B_r would be in vacuum. When equilibrium force balance is reached the electron slip will adjust so that $\delta^* \approx \Delta r$, just the penetration distance needed to carry the equilibrium line current. The azimuthal current for the inner field lines is driven by inward diffusion, and the analytic models assume an overall inward velocity throughout the FRC. The RMF on the outer field lines must be strong enough to both drive current there, and also produce the inward flow necessary to drive the inner field line current. Either a source of particles near the sepa-

ratrix, or a net circulation from inner to outer field lines, driven by pressure differences along the same flux surfaces, is thus an implied assumption of the simple models, and is most likely required for steady-state operation. The latter process is utilized in the numerical MHD calculations.[11]

Using the above equations the azimuthal current drive force is seen to be

$$F_{M\theta}=\langle j_z B_r\rangle=\frac{2B_\omega^2}{\mu_0 a}\left(\frac{a}{r}\right)^2 e^{-[2(a-r)/\delta^*]}. \tag{6}$$

At the plasma edge this is seen to be independent of penetration distance since greater penetration increases both E_z and B_r, but reduces the slippage and the (ϖ/ω) term governing j_z. For steady-state current drive, the total torque applied by the RMF, $T_M=\int_0^a 2\pi r^2 F_{M\theta}\,dr$, must be balanced by the resistive torque, $T_\eta=\int_{a-\delta^*}^a 2\pi r^3 m_e n_e \nu_\perp \omega_r\,dr$ where $\nu_\perp$ now represents the effective cross-field electron–ion collision frequency. This results in the following basic relationship:

$$\gamma/\lambda \approx 1/\sqrt{2} \tag{7}$$

when the ratio is written in terms of the peak density, assuming $a\sim r_s$, $\omega_r\sim\omega$, and $\delta^*\ll a$. This approximate result can be seen using Eqs. (31) and (32) of Ref. 7, recognizing that γ in that paper is based on the average density in the current sheet, $\sim 0.5 n_{em}$, making γ twice as large as the value used here. There are many three-dimensional effects that make this relationship only an approximate one, but it is nevertheless useful for scaling. It will be used in evaluating effective values of $\eta_\perp$ in the experiments.

The RMF also produces an inward force $F_{Mr}=\langle j_z B_\theta\rangle$. This can be integrated from the plasma center to edge, yielding the approximate result

$$p_{\mathrm{RMF}}=\frac{B_\omega^2}{\mu_0}e^{-[2(a-r)/\delta^*]}. \tag{8}$$

It can be seen from Eq. (5) that B_θ at the plasma edge is twice B_ω (due to the axial shielding currents in the plasma), but the effective pressure contribution is only one-half $(2B_\omega)^2/2\mu_0$ due to the oscillating nature of B_θ. Equation (8), or p_{RMF} based on the measured $B_\theta(r)$, will be used in the radial pressure balance relationship

$$p(r)+\frac{B_z^2(r)}{2\mu_0}+p_{\mathrm{RMF}}=\frac{B_e^2+2B_\omega^2}{2\mu_0} \tag{9}$$

to determine the internal pressure profiles from measured values of $B_z(r)$ and $B_\theta(r)$.

Numerical values of the equations to be used in evaluating experiments are listed below. The units for $D_\perp=\eta_\perp/\mu_0$ are m^2/s and for n_{em} are $10^{20}\ \mathrm{m}^{-3}$. In addition, ω is in 10^6 rad/s, and r_s in m. The simple analytic relationship used for evaluating the ability to form a given FRC is obtained by setting $\gamma/\lambda=1/\sqrt{2}$. In numeric units,

$$\frac{\gamma}{\lambda}=\frac{0.007B_\omega(\mathrm{G})}{n_{em}(D_\perp\omega r_s^2)^{1/2}}=\frac{1}{\sqrt{2}}. \tag{10}$$

This may be used to evaluate effective cross field resistivities, i.e.,

$$D_\perp(\mathrm{m}^2/\mathrm{s})=\frac{(B_\omega(\mathrm{G})/100)^2}{n_{em}^2(\omega r_s^2)}. \tag{11}$$

It will be seen that this value differs by less than a factor of 2 from that inferred by measured power absorption. Based on the analytic formula, for a given resistivity the peak density will thus scale as

$$n_{em}(10^{20}\ \ \mathrm{m}^{-3})=0.01B_\omega(\mathrm{G})/(D_\perp\omega r_s^2)^{1/2}. \tag{12}$$

The resultant external field will depend on the degree of RMF penetration

$$B_e(T)=10\left(\frac{\Delta r}{r_s}\right)n_{em}(\omega r_s^2). \tag{13}$$

Using Eqs. (2) and (12), this can be expressed as

$$B_e(T)=\frac{(\omega r_s^2)^{1/2}B_\omega(\mathrm{G})\langle\beta\rangle\zeta}{20D_\perp^{1/2}}. \tag{14}$$

For a given resistivity and (ωr_s^2), both the density and the final external field are predicted to scale linearly with RMF strength B_ω. For the magnetic field, this assumes that the drive efficiency parameter $(\Delta r/r_s)$ or ζ remains constant. This is somewhat misleading, because if the plasma temperature could be increased, the density would decrease, and it would be possible to increase the RMF frequency ω while maintaining the same ζ. In the actual experiments, when ω was decreased to increase ζ, there was only a marginal increase in B_e. This is not surprising given the weak dependence on ω implied by Eq. (14) and a somewhat higher density obtained at smaller ω. It was mainly possible to reach higher values of external field due to the lowered circuit impedance and resultant ability to produce higher values of B_ω. However, for a given value of B_ω, the lower ω operation with resultant larger ζ and thicker current carrying region, did result in significant drops in power absorption.

III. INITIAL OPERATION AT $\omega=10^6$ rad/s

A. TCS description and operation

RMF current drive has been applied to the TCS device, producing nearly steady state FRCs with configuration lifetimes over several milliseconds, limited only by the applied RMF duration. The TCS facility is described elsewhere,[4] but a vertical cross section of the RMF current drive chamber is shown schematically in Fig. 1. There are two pairs of RMF antennas, situated at a radius of 54 cm, outside the quartz vacuum vessel and the axial confinement coils. The vertical and horizontal fields produced by the antennas oscillate 90° out of phase, generating a uniform RMF inside the 80 cm diameter quartz chamber as sketched on Fig. 2. The confinement coils consists of 20 56-turn coils with an effective flux confinement radius of $r_c=47$ cm. These coils act as a flux shaper because individual sets of 14 and 6 (three at each end) coils are each fed in parallel, and also as a flux conserver because the external capacitor bank supply inductance is low. The coils under the RMF antennas are employed to produce

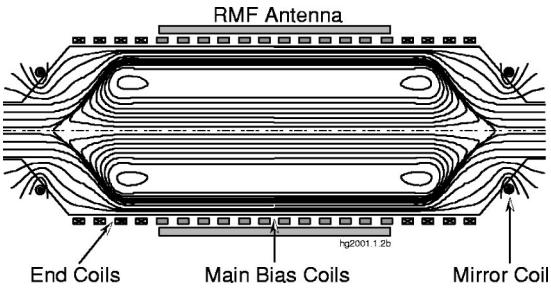

FIG. 1. Side view of the TCS RMF current drive chamber. Positions of the different bias coils and the RMF antennas are indicated.

the main bias field, while the coils located at the ends can be powered separately to allow for FRC shaping control. The ends of the TCS chamber consist of stainless steel lined conical sections to link to 27 cm input and exit sections. Mirror coils provide additional axial confinement.

The initial RMF experiments were conducted in TCS with the RMF operated at $\omega = 10^6$ rad/s. The RMF was applied to a preionized deuterium gas in a uniform bias field to form FRCs and, subsequently, maintain the configuration. The FRCs obtained during this campaign had relatively low electron densities, i.e., $n_e \sim 10^{19}$ m^{-3}, with temperatures below 60 eV, as derived from radial pressure balance. Figure 3 shows the time evolution of such an FRC produced by the RMF. B_e is the external axial magnetic field at the midplane, measured by normal magnetic pick-up loops mounted on the quartz vacuum vessel beneath the axial confinement coils. B_{int} is the internal axial field at $r=11$ cm, inside the field null, obtained from an internal magnetic probe. The peak density, n_{em}, is determined from the measurements of a double pass CO_2 interferometer allowing for profile effects,

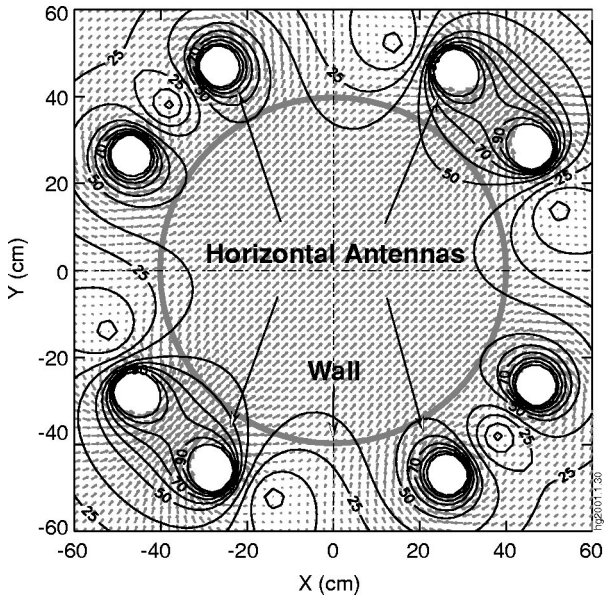

FIG. 2. RMF field uniformity inside the TCS chamber with a field angle at 45 degrees from X axis. The magnitudes of the field strength, as indicated by the contour levels in the unit of G, are calculated with a circulating current of ± 9 kA in the horizontal and vertical antennas, which corresponds to a ± 10 kV pulsar voltage at an RMF drive frequency $\omega = 1.0 \times 10^6$ rad/s. Locations of the horizontal field antennas are also indicated.

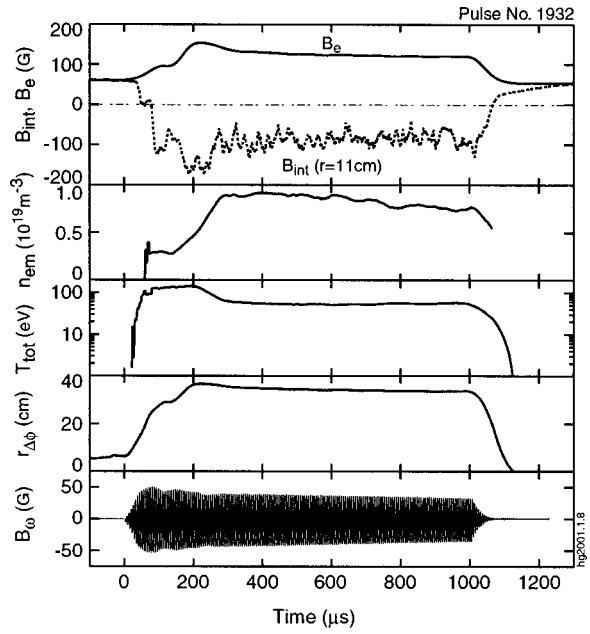

FIG. 3. Example of a steady state FRC produced by the RMF alone at $\omega = 10^6$ rad/s. The time traces represent the plasma behavior at the axial midplane. The plotted B_ω is actually the vertical antenna current multiplied by 6.4 G/kA.

i.e., $n_{em} = \int n_e \, dl / 4\langle\beta\rangle r_{\Delta\phi}$. $\langle\beta\rangle = 1 - 0.5 x_s^2$ is calculated from the standard, flux confined, elongated FRC relationship for this and other discharges even though this may not apply exactly for the antimirror or mirror end conditions as discussed in Secs. III C and IV A. However, there is insufficient data in the end region to apply a more accurate analysis,[15] and the principal results of this paper will only be marginally affected by small changes in the assumed $\langle\beta\rangle$. The total temperature at the field null, $T_{\text{tot}} = T_e + T_i$, is inferred from pressure balance taking into account the contribution from the RMF radial confining force, $T_{tot} = (B_e^2 + 2B_\omega^2)/2\mu_0 n_{em}$, as obtained from Eq. (9). The excluded flux radius, $r_{\Delta\phi}$, is calculated from the measured excluded flux, $\Delta\phi$, and external magnetic field, $r_{\Delta\phi} = (\Delta\phi/\pi B_e)^{1/2}$. For a standard FRC this should be approximately equal to the separatrix radius r_s. B_ω is the vacuum RMF obtained from the measured zero to peak antenna current $B_\omega(\text{G}) = 6.4 I_{\text{ant}}(\text{kA})$.

The discharge shown in Fig. 3 was initiated with an RMF of $B_\omega = 50$ G and a bias field of $B_0 = 60$ G. Azimuthal current was driven and the internal field was rapidly reversed, forming an FRC. The plasma rapidly expanded radially, compressing and heating the plasma to over 100 eV and raising the external field to about 150 G. For these high ω shots either the ionization rate was relatively slow, or the plasma accumulation rate was high, so that the density continued to increase. This resulted in a decrease in temperature and external field. The decrease in B_e is assumed due to increased electron ion friction in the γ/λ relationship, which is reflected in a lower value of ζ in Eq. (14). A quasisteady equilibrium is established with $B_e \sim 120$ G by 300 μs, with further decay due mainly to decay in the RMF (supplied by a capacitor bank).

During equilibrium the separatrix had a radius of about

36 cm, which is 4 cm inside the vessel wall, and an x_s value of 0.77. The plasma density at the field null n_{em} was 0.9 $\times 10^{19}$ m^{-3}, and the total temperature, $T_{\rm tot}$, was about 55 eV. It is to be noted that Doppler broadening measurements have shown that ions are cold for the low density RMF formed FRCs.[16] Thus the value of temperature inferred from radial pressure balance can be largely ascribed to the electron temperature.

The amount of RMF penetration is related to the achieved external field and the plasma density through Eq. (1). For the shot shown in Fig. 3, Δr is only about 4 cm, which is consistent with internal field profile measurements. The effective diffusivity can be estimated from Eq. (11) to be 135 m^2/s, which is nearly 20 times the classical value. More results on the inferred anomalous diffusivity for the steady state discharges at $\omega = 10^6$ rad/s are given in Sec. IV A where comparisons are made with the reduced ω discharges.

One critical issue with RMF current drive is ion spin-up in the RMF direction due to collisions with electrons, thus reducing the RMF current drive efficiency. An ICCD (intensified charge coupled device) camera has been employed to routinely determine Doppler shifts of low charge state impurity ions, viewing the plasma midplane on a number of lines of sight with different impact parameters.[16] It has been found that the ions rotate in the same direction as the RMF, as expected. However, the ions are spun up to a frequency of only about 6 kHz, much smaller than the RMF drive frequency of 180 kHz, most likely due to retarding collisions with neutrals that are present in the FRCs. This is addressed in Sec. IV F, along with comparisons with the results from the reduced ω campaign.

B. Role of main bias

For an FRC formed by the RMF and confined in a flux conserver, the final equilibrium is also dependent on the initial bias field due to the flux conservation relationship $B_0 r_c^2 = B_e(r_c^2 - r_s^2)$. In order to investigate the effect of the initial bias field, we have carried out a series of dedicated experiments with the RMF operated at the same pulsar voltage (14 kV) but the bias field varied between 20 and 90 G. Figure 4 shows the time evolution of three comparable discharges started with different bias fields. As can be seen, in the lowest bias case, the excluded flux radius, $r_{\Delta\phi}$, is outside the quartz vessel wall, which limits the FRC radial expansion. The external field, B_e, is thus relatively low. The applied bias field is sufficiently raised in pulse 2412 so that the FRC never reaches the wall and the external field reaches a maximal value. As the bias field is further increased (pulse 2401), the current drive is insufficient to produce an equal magnitude internal field and the excluded flux radius is small. The line averaged electron density, $\langle n_e \rangle$, however, is comparable to the other two discharges.

More results are shown in Fig. 5 where the external and internal fields, and the excluded flux radius are plotted against the initial bias. $r_{\Delta\phi}$ is assumed to accurately represent the separatrix radius r_s. While the internal field remains reversed x_s and $\langle \beta \rangle = 1 - 0.5 x_s^2$ are also shown. The data are taken from a series of similar discharges including the pulses

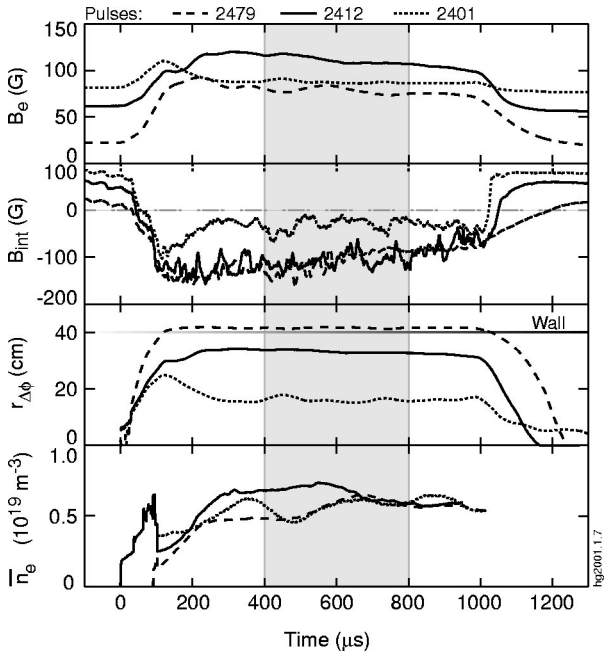

FIG. 4. Time traces of midplane quantities for three comparable discharges with different initial bias fields. The data shown are the external axial field B_e, the internal axial field $B_{\rm int}$ at $r=2$ cm, the excluded flux radius $r_{\Delta\phi}$, and the line averaged density $\langle n_e \rangle$ obtained from a double pass CO_2 interferometer across the diameter in the center of TCS.

shown in Fig. 4 and are averaged over the time window between 400 and 800 μs (as highlighted in Fig. 4). For optimal results the bias field strength should be chosen in accordance with the RMF drive strength to allow for the FRC to expand close to, but not beyond the plasma tube wall.

C. Influence of end fields

As in conventional field reversed theta pinch (FRTP) formed FRCs, RMF formed FRCs also exhibit rotational in-

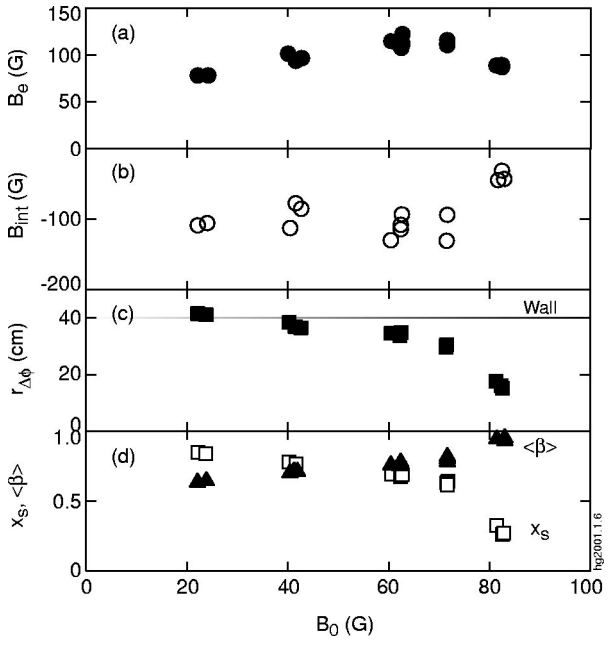

FIG. 5. Dependence on the bias field of (a) external axial field B_e, (b) internal axial field $B_{\rm int}$, (c) excluded flux radius $r_{\Delta\phi}$, (d) x_s, and $\langle \beta \rangle$.

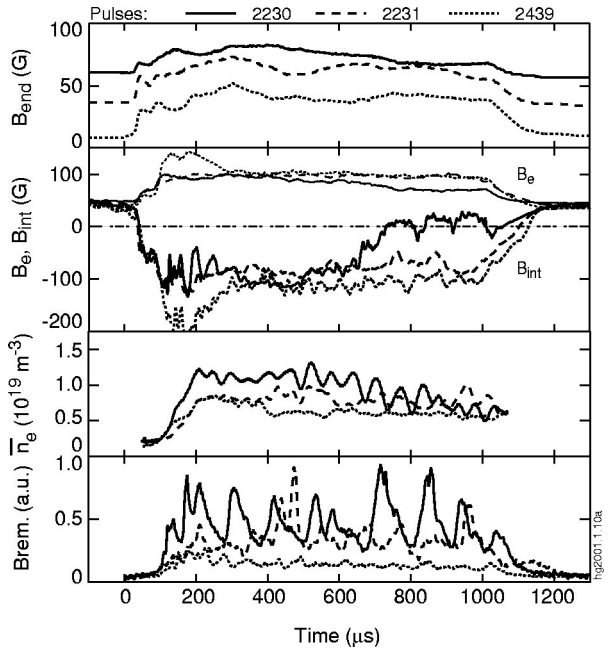

FIG. 6. Comparison of three discharges with successively increased end fields. The data shown are the field measured at the end of the TCS confinement chamber (B_{end}), the external (B_e) and internal (B_{int}) magnetic fields, the line averaged density, $\langle n_e \rangle$, as well as traces from edge tomography at the axial midplane.

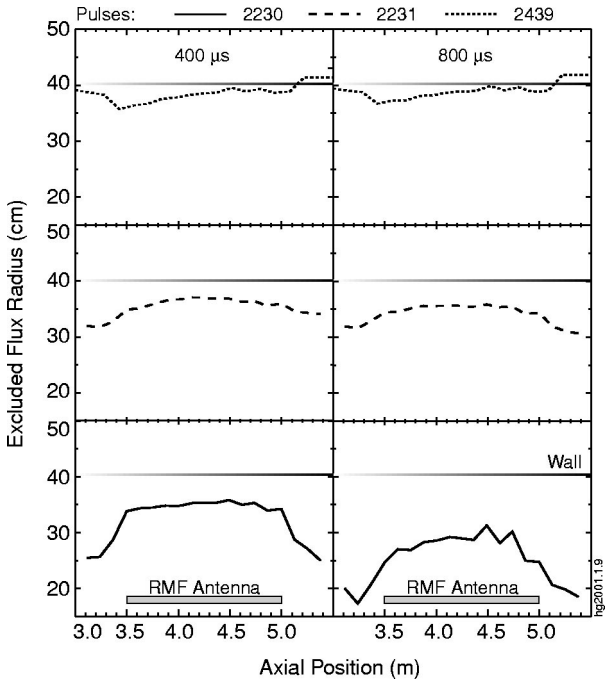

FIG. 7. Excluded flux radius as a function of axial position for the discharges shown in Fig. 6 at 400 and 800 μs, respectively.

stabilities, which have proven to be very sensitive to the applied bias fields. To obtain the oscillation-free steady state FRCs shown earlier, we have had to limit the bias field strength at the ends to lower than the main bias field strength in the region under the RMF antennas. To illustrate this, Fig. 6 shows time traces for three discharges with the same main bias field but different end fields. For all the $\omega = 10^6$ rad/s discharges the mirror coils shown in Fig. 1 were not used, so that the FRC could extend to the end cones when the end coils produced less flux than the main bias coils. It can be seen that for the lowest end bias case (pulse 2439), the internal magnetic field is fully reversed by the RMF and the configuration is maintained in steady state until termination of the applied RMF at 1000 μs. When the end field is raised to near the main bias field level (pulse 2231), rotational instabilities develop (as indicated by the oscillations on the implied density and edge bremsstrahlung measurements) early in the discharge and remain until the end of the discharge, but the configuration is maintained. The modes are aggravated in pulse 2230, as the end bias field is further increased, accompanied by the loss of the reversed inner field (B_{int}) at 700 μs. The instabilities manifest themselves predominately as $n=1$ off-center rotation, accompanied by the $n=2$ mode, as identified by edge tomography and an array of external magnetic probes. The modes rotate in the RMF direction at a frequency around 10 kHz, much slower than the RMF rotational speed, but about equal to the measured ion rotation rates.

It is not evident that the rotational instabilities are entirely responsible for the loss of the configuration in the strong end field case (pulse 2230). As can be seen from the time traces for the density and edge bremsstrahlung measurements shown in Fig. 6, the modes are present at the very beginning of the discharge, and do not show obvious growth before the loss of the field reversal. To the contrary, the edge radiation exhibits strong oscillations when the inner reversed field is lost.

Another reason for the loss of flux reversal might be related to an inability to sustain a required inward radial flow, as described in Sec. II. When the end bias field is sufficiently low, FRCs extend beyond the RMF antennas (pulse 2439), forming a barbell-like configuration with some wall contact, as indicated by Fig. 7. This might facilitate the necessary separatrix particle inflow near the separatrix, either through an enhanced neutral background or a swirling flow around the FRC ends from the inner field lines to the outer region. In contrast, increasing the end fields compresses the FRC axially towards the region under the RMF antennas, perhaps restricting circulation of particles.

Too low end fields tend to cause axial asymmetry, leading to wall contact at the ends. Operation at the reduced RMF frequency ($\omega = 0.5\times10^6$) appears to be less sensitive to the end field strength, hence a strong end bias can be applied for additional axial confinement, as will be further discussed in Sec. IV A.

D. Edge magnetic field oscillations

The internal magnetic field time history for shot 2439 (low end fields) is shown on Fig. 8. It is rather striking that there are strong oscillations near the edge even though the FRC is otherwise free of global rotational modes. Numerical simulations using a 2D RMF code[11] suggest that this might be attributed to a low value of ζ equal to only 0.24. With low ζ, the RMF can only penetrate into a thin edge layer which tends to lead to unsteady current drive. This is illustrated by

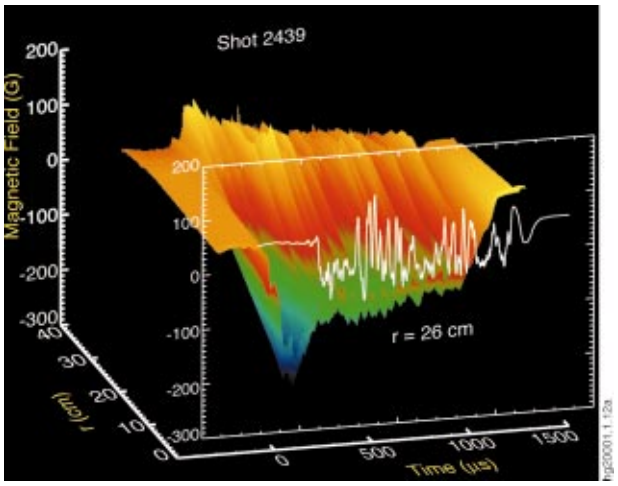

FIG. 8. (Color) Axial magnetic fields as a function of radius and time for pulse 2439, showing strong oscillations at the FRC edge. Also shown is a time trace of the magnetic field at $r = 26$ cm (near the field null).

the MHD calculation on Fig. 9 where profiles of the axial magnetic field, B_z, along with the corresponding RMF field lines are shown for a case with $\zeta=0.28$. (a) Initially the RMF easily penetrates enough to reverse the initial bias field. (b) As further current and flux are produced the plasma expands, increasing the external field and the density until there is insufficient RMF drive near the field null to sustain synchronous rotation there. (c) The inner RMF then tears and the process can repeat itself.

In order to improve the RMF current drive efficiency, we have carried out an experimental campaign with the RMF operated at one-half of the original frequency, i.e., $\omega=0.5\times10^6$ rad/s in order to increase ζ. The results from the reduced ω experiments are presented in the next section and

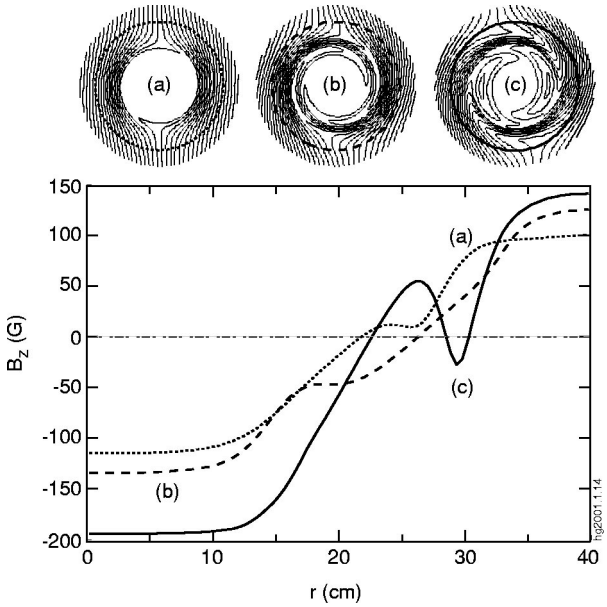

FIG. 9. Simulation profiles of the axial magnetic field, B_z, along with the corresponding RMF field lines, for three different times to illustrate unstable RMF current drive at low ζ.

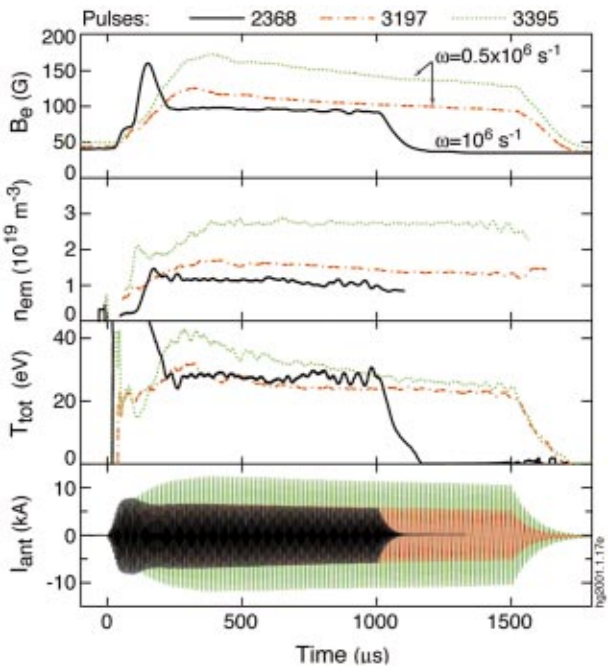

FIG. 10. (Color) Comparison of the discharges with RMF operated at $\omega = 10^6$ and 0.5×10^6 rad/s to illustrate the effect of ω at similar RMF field strengths, and the consequence from the increase in the antenna current at similar RMF pulsar voltages. Time traces shown are for three pulses: (1) pulse 2368 at 10^6 rad/s, 14 kV; (2) pulse 3395 at 0.5×10^6 rad/s, 14 kV; (3) pulse 3197 at 0.5×10^6 rad/s, but at 8 kV to match the RMF field strength in 2368.

detailed comparisons are also made with the high ω experiments.

IV. RESULTS AT REDUCED RMF FREQUENCY: $\omega=0.5\times10^6$ rad/s

A. Direct consequence of reduced ω

Figure 10 compares the discharges obtained with the RMF operated at $\omega=10^6$ and 0.5×10^6 rad/s. Pulse 2368 at $\omega=10^6$ and pulse 3197 at $\omega=0.5\times10^6$ have the same RMF field strength, as indicated by the antenna current, I_{ant}, and the same initial bias field. As can be seen, the reduced ω discharge shows an increase of ~30% in the FRC peak density compared to the higher ω discharge, as predicted by the steady state RMF current drive requirement [Eq. (12)] assuming a similar cross-field diffusivity, $D_\perp$, for this pair of discharges. The external magnetic field is also increased, suggesting more efficient RMF current drive, as expected at higher ζ. The total temperature, determined from radial pressure balance is similar for the two discharges. The difference in start-up behaviors is due to differences in particle inflow or ionization rates. At the higher RMF frequency ionization occurs less rapidly, allowing transiently higher temperatures, lower densities for a given external field and reduced electron ion friction even assuming constant $\eta_\perp$.

Reducing the RMF frequency reduces the impedance (ωL) of the antenna tank circuit, which allows for a higher antenna current, at a given pulsar voltage. This, in turn, leads to a higher external magnetic field that can be sustained by the RMF and an increase in the electron density, as expected

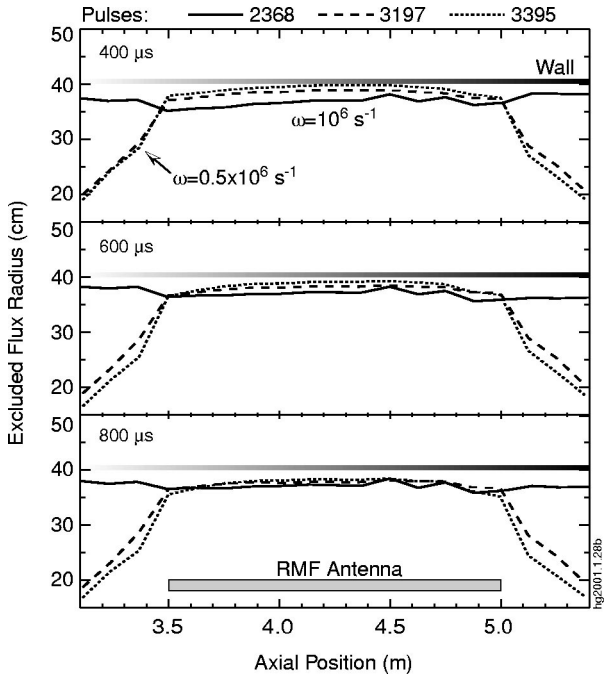

FIG. 11. Axial excluded flux profiles at different times for the three discharges shown in Fig. 10. The axial location of the RMF antennas is also indicated.

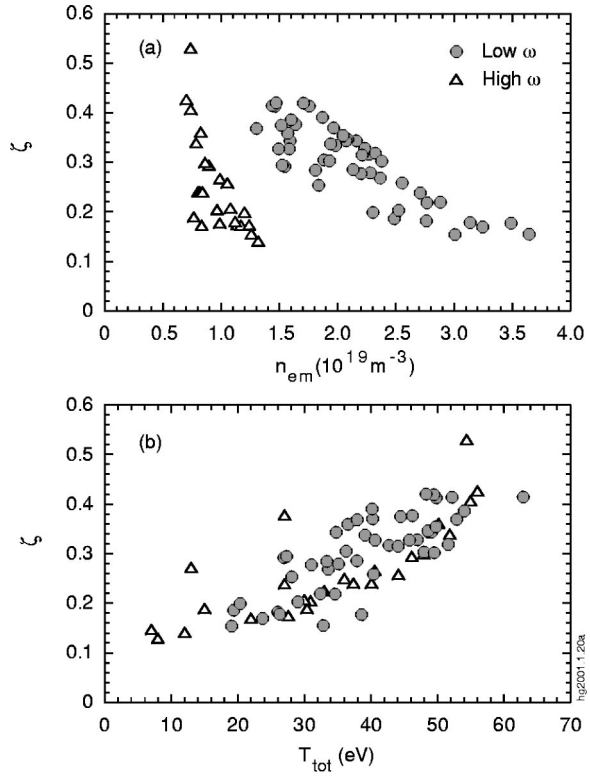

FIG. 12. ζ versus (a) plasma peak density and (b) peak temperature derived from radial pressure balance.

[see Eqs. (12) and (13)]. To illustrate this, in Fig. 10 are also shown the time traces for another reduced ω discharge, pulse 3395, which was operated at the same pulsar voltage as its high frequency counterpart (pulse 2368). It can be seen that the RMF antenna current is doubled, consistent with the changes in antenna impedance. This, along with the reduced ω, results in a significant increase in the density and the external magnetic field, although only a modest increase in plasma temperature.

One unexpected result from the reduced ω campaign is that the FRCs appear to be less sensitive to the end field configuration. Figure 11 shows the excluded flux radius as a function of the axial position for the above three discharges. In both reduced ω (3197 and 3395) discharges, strong end fields have been applied, using both the end coils and mirror coils of Fig. 1, to ensure the axial symmetry of the FRCs. In contrast to the high ω (2368) discharge which has a lower end bias and no mirror fields to allow the FRC to extend axially beyond the RMF antennas, in both the reduced ω discharges the FRCs appear to be restricted axially primarily to the region under the RMF antennas. Thus, it might be difficult to establish a swirling flow around the FRC ends to sustain the inward velocity required to reverse the axial fields inside the field null. Yet, a fully reversed configuration is obtained and maintained during the entire RMF phase. Such an inward flow is therefore most likely sustained by the localized ionization of neutrals in the region near the field null, as mentioned in Ref. 4. High plasma densities in the reduced ω discharges limit the neutrals to the edge region where the strong RMF drive occurs. In the high ω discharges, plasma densities are low, so that neutrals have large mean free paths and are present over the entire volume of the plasma. In that case, the particle source at the edge may not be sufficient to provide the required inward flow, and a swirling flow at the FRC ends would be necessary to sustain RMF current drive in steady state.

B. RMF current drive efficiency and diffusivity scaling

The toroidal current driven by the RMF is dependent on both the degree of RMF penetration (ζ) and the cross-field resistivity ($D_\perp$) for a given RMF frequency and a given field strength. The resultant external field is given in Eq. (14). Figure 12 plots ζ derived from Eq. (1) against (a) plasma peak density and (b) temperature derived from radial pressure balance. These results were obtained from varying B_ω, and to some degree by changing the puff fill conditions. The data are obtained from the steady state phase of the discharges with the RMF operated at both 10^6 and 0.5×10^6 rad/s. It is evident that ζ increases at lower ω for a given density, but the primary effect of halving ω was to double the density and maintain a similar ζ. An obvious way to increase ζ and the RMF current drive efficiency would be to raise the plasma temperature. This will be done in future experiments with translated the pinch formed FRCs.

Figure 13 plots B_e, which can be sustained by the RMF, as a function of B_ω. A result from STX[5,6] is also shown for comparison. As can be seen, B_e shows a nearly linear dependence on the RMF field, independent of ω. This is to be expected from torque balance considerations since the RMF force [Eq. (6)] does not depend on ω. The RMF penetration depth will adjust as needed to carry the FRC current. STX operated at the same ωr_s^2 as TCS, $\omega=2.2\times10^6$ rad/s and $r_s=20$ cm, but better vacuum conditions led to relatively

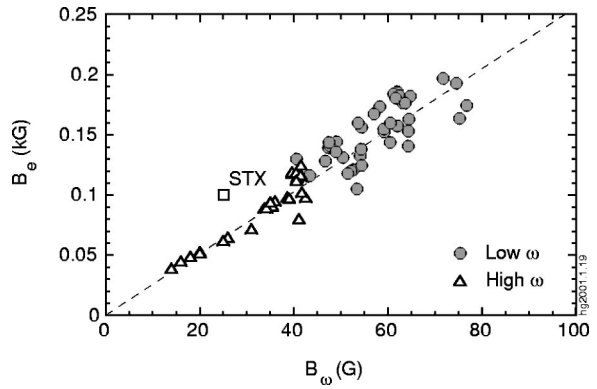

FIG. 13. B_e versus B_ω for the discharges obtained with RMF operated at $\omega=10^6$ and 0.5×10^6 rad/s. The data were obtained in the steady state phase around 500 μs and are averaged over a time window of 200 μs. An STX example, although not in steady state, is also included.

higher temperatures, lower densities (as in the transient condition shown on Fig. 3), and thus higher ζ, yielding better scaled performance. To further improve performance, at a given RMF field, it is essential to both increase the plasma temperature and reduce the anomalous diffusivity.

For steady state FRCs, the effective diffusivity can be derived from the approximate γ/λ relationship of Eq. (11). Figure 14(a) shows the derived diffusivities for the steady state discharges with $\omega=10^6$ and 0.5×10^6 rad/s. The prediction from conventional high density (LSX) FRC scaling, $D_\perp \approx 11.2 x_s^{-1/2} r_s^{-0.14} n_{em}^{-1/2}$, is also shown.[8] Not only is the inferred resistivity higher, at least for low densities, than the LSX scaling, but a simple $D_\perp \sim 1/\sqrt{n}$ relationship does not appear to hold. A better result is obtained when $D_\perp$ is plotted versus the Bohm value, as shown in Fig. 14(b). It is to be noted that the diffusivity obtained for previous hot, translated FRCs[4] was nearly a factor of 10 lower than the data from present RMF formed FRCs, and even fell well below the high density LSX scaling. This suggests that the higher diffusivity seen in the present RMF formed FRCs, compared to the conventional FRCs, may be due to a lack of hot ions, or perhaps to the present operation with relatively large B_ω/B_z values. We are planning to apply RMF current drive at low values of B_ω/B_z to the translated hot FRCs to investigate this.

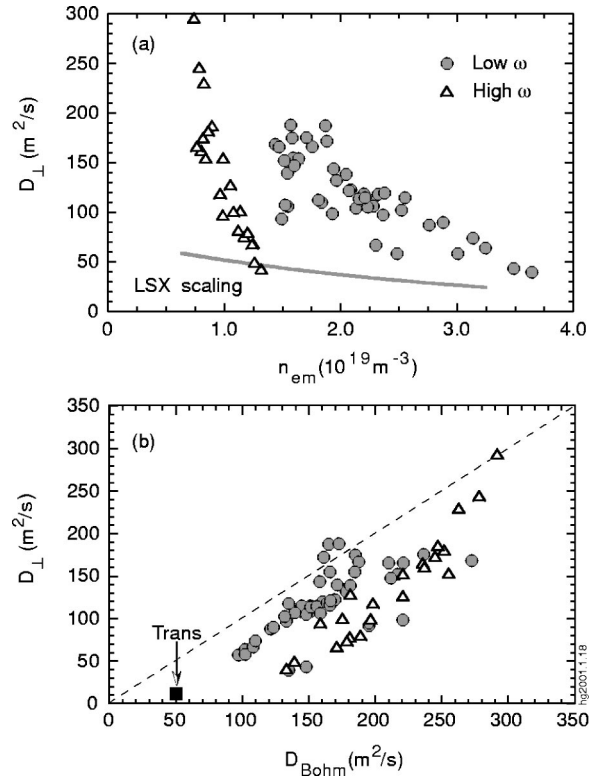

FIG. 14. Cross field diffusivity based on Eq. (11) (a) versus n_{em}; (b) versus $D_{\rm Bohm}$ $[D_{\rm Bohm}=625T_e({\rm eV})/B({\rm G})]$ for different ω cases. Conventional high density FRC scaling (LSX) and data from the translated FRCs obtained previously in TCS are also shown (square symbol).

C. Internal profiles

As expected, reducing the RMF frequency facilitates RMF current drive and reduces the edge magnetic oscillations, thus permitting us to carry out detailed measurements of the internal magnetic fields of the FRC. To illustrate this, Fig. 15 shows the time traces of the edge magnetic fields outside the field null, along with the inner field at $r=2$ cm, for a typical steady state discharge produced by the RMF at $\omega=0.5\times10^6$ rad/s. In addition, Fig. 15 shows the excluded flux radius and the line averaged density. The oscillations of the edge magnetic fields are significantly reduced, compared to the FRCs obtained during the high ω campaign (Fig. 8). Detailed radial and axial profiles of both B_z and the RMF B_θ for such FRCs have been obtained from two moveable magnetic probes situated at the midplane and the end of TCS. The probes consist of a series of magnetic pick-up loops inside a 2 mm diameter beryllia (BeO) tube. There was no difference in overall FRC parameters with and without this small internal probe.

Figure 16(a) shows the radial profiles of measured B_z and B_θ, along with the calculated RMF fields (B_θ and B_r) based on Eqs. (4) and (5). The parameter a is taken as $0.9r_s$ and $\delta^*=4$ cm in the analytic expressions. The radial location of the axial field null ($R=29$ cm), the separatrix radius ($r_s=39$ cm), as well as the radial position of the vacuum vessel, are also shown. The data are obtained and averaged between 600 and 700 μs during the steady state phase of a series of identical discharges. For these experiments the measured antenna current would produce a B_ω value of 60 G in vacuum, and this value is nearly doubled at the plasma edge ($B_\theta \approx 2B_\omega$), due to axial screening currents, in accordance with Eq. (5).

The B_θ measurements show that the RMF just penetrates to the field null, about 10 cm inside the separatrix (r_s). This is a natural consequence of steady state RMF current drive of FRCs in flux conservers, as described in Sec. II. It can be seen that current is also maintained on the inner field lines. Since the θ component of the generalized Ohm's law can be written as

$$E_\theta = \eta_\perp j_\theta + u_r B_z + \langle j_z B_r \rangle / ne, \tag{15}$$

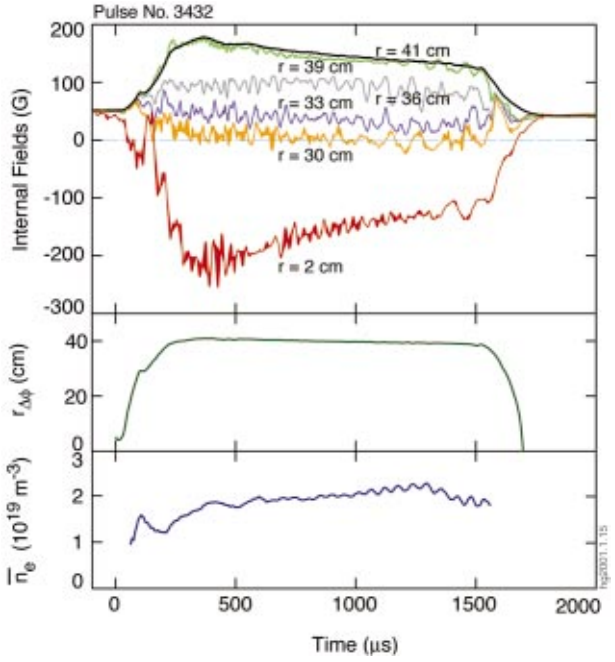

FIG. 15. (Color) Time traces of the magnetic field external to the vacuum vessel and at various internal radii measured at the axial midplane. Also shown are the excluded flux radius, $r_{\Delta\phi}$, and the plasma line averaged density, $\langle n_e \rangle$, for a steady state FRC produced by the RMF with $\omega = 0.5 \times 10^6$ rad/s, $B\omega = 60$ G.

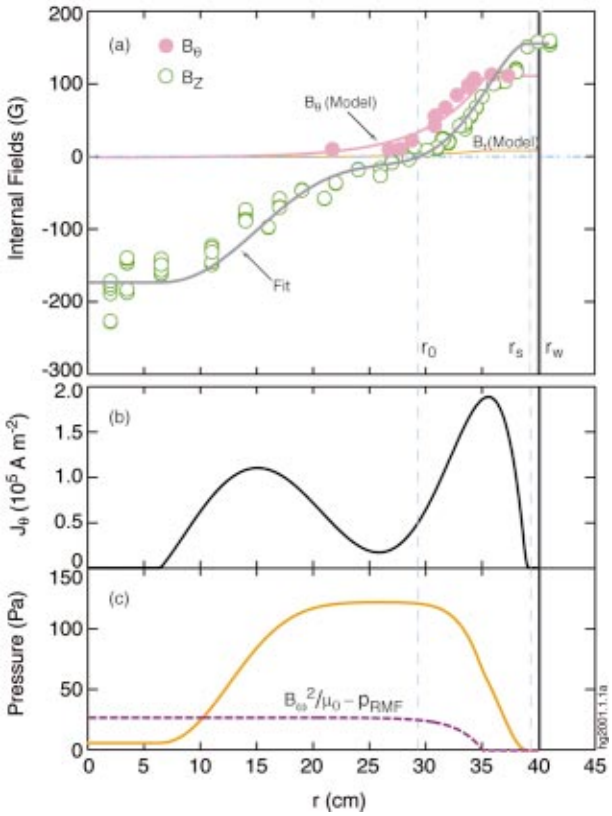

FIG. 16. (Color) Radial profiles of steady state FRCs produced by RMF: (a) measured axial magnetic field B_z and RMF field B_θ, as well as analytic calculations of B_θ and B_r; (b) toroidal current j_θ derived from a ninth order polynomial fit to the B_z data; (c) plasma pressure obtained from radial pressure balance taking into account RMF contribution. The contribution from the RMF, $B_\omega^2/\mu_0 - p_{\mathrm{RMF}}$, is also shown.

and in steady state E_θ must be equal to zero everywhere, the azimuthal current can only be maintained by an inward velocity, i.e.,

$$j_\theta = u_r B_z / \eta_\perp . \tag{16}$$

In this expression, B_z is also negative for the inner field lines. Actually, u_r represents an inward electron velocity and it is not necessary that the ions follow. A swirling flow from the inner field lines to the outer field lines can maintain particle or current continuity. A swirling current would produce some toroidal field, but we have not yet attempted to measure this. Swirling particle flow might lead to a significant loss of particles at the ends near the *X*-point where fields are small and ion gyroradii are larger. In that case, lost particles must be balanced by ionization of recycling or background neutrals in the region outside the field null. The consequence of this for energy losses is discussed in Sec. IV E.

Figure 16(b) shows the FRC current profile derived from a ninth-order polynomial fit to the B_z profile data. The FRC is about 2 m long and the total toroidal current driven by the RMF is about 50 kA in this particular operating condition. As can be seen, the profile peaks near the edge and requires little RMF current drive near the field null. This is a unique feature of RMF driven FRCs.[5,6] As a result, the poloidal flux, $\phi_p = \int_R^{r_s} B_z 2\pi r\, dr$, is reduced compared to that for conventional FRCs produced by the field reversed theta pinch (FRTP) method. For example, ϕ_p calculated from the $B_z(r)$ profile shown in Fig. 16(a) is about 1.6 mWb, which corresponds to the value given by $\phi_p = (x_s^2/\sqrt{2})^{1+\varepsilon} \pi R^2 B_e$ with $\varepsilon \approx 0.8$, approaching the Lowest Flux Sharp Boundary (LFSB) solution,[17] while a typical rigid rotor profile would yield a poloidal flux: $\phi_p = 0.62 x_s \pi R^2 B_e \approx 2$ mWb.

It is interesting to note that the magnitude of axial field strength at the center is higher than the strength of the external magnetic field, which is measured just outside the quartz vacuum vessel wall. This is simply a consequence of Eq. (9) where $p_{\mathrm{RMF}} = 0$ on the inner field lines. For $B_\omega = 60$ G, $B_e = 160$ G, the internal field would be about 175 G if $p(0) = 0$.

Using the analytic expression for p_{RMF} in Eq. (8), the radial pressure can be calculated from the measured values of $B_z(r)$ using Eq. (9). The results are shown in Fig. 16(c). In particular, the contribution $B_\omega^2/\mu_0 - p_{\mathrm{RMF}}$ from the RMF confining force, i.e., $\langle j_z B_\theta \rangle$, is also shown. As discussed earlier, in the presence of a flux conserver, only partial penetration of the RMF (up to the field null) will occur. This increases B_θ above the vacuum value, and can contribute significantly to the plasma pressure, and thus confinement.

From the pressure profile shown in Fig. 16(c), we can calculate the average β of the FRC: $\langle \beta \rangle = (2\int_0^{r_s} pr\, dr / r_s^2)/((B_e^2 + 2B_\omega^2)/2\mu_0) \approx 0.69$, which is close to the value derived from the axial force balance between field line tension and plasma pressure $\langle \beta \rangle = 1 - 0.5 x_s^2 = 0.66$.[18] It may be noted that, although B_ω is only about one-third of the final external axial field, B_e, the RMF azi-

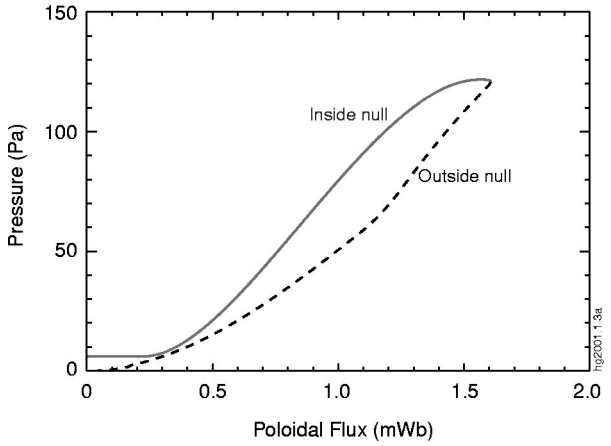

FIG. 17. Plasma pressure versus poloidal flux, including contribution from RMF radial confining force $\langle j_\theta B_z \rangle$.

muthal field $B_\theta(r)$ is actually larger than $B_z(r)$ over much of the outer flux surfaces. However, as can be seen from the curve for $B_r(r)$ on Fig. 16(a), the radial field, which determines the $\langle j_z B_r \rangle$ current drive, is very small. A large value of B_θ/B_z, though beneficial to radial confinement, should thus not be necessary for RMF flux sustainment. Since one worry about RMF current drive is that it opens up field lines, even if only in a fluctuating manner, it is encouraging that the value of B_r is only a small fraction of the generated axial field B_z.

The pressure as a function of the poloidal flux is shown in Fig. 17. As can be seen, the pressure on the inner flux surfaces is higher than that on the corresponding outer flux surfaces. This cannot be due to local heating since RMF power is predominately deposited in the edge layer outside the field null. This higher pressure on the inner field lines is consistent with numerical models of inwardly driven flow, with the pressure difference along flux surfaces resulting in an assumed swirling flow.[11]

An attempt has been made to reproduce the experimental results with a 2D RMF current drive code developed by Milroy.[11] Figure 18 shows the computed radial profiles of the axial field, $B_z(r)$, the RMF field, $B_\theta(r)$, as well as the radial flow, $u_r(r)$, driven by the RMF. The key input parameters used in the computation are as follows: RMF $\omega = 0.55 \times 10^6$ rad/s, $B_\omega = 60$ G; and an anomalous resistivity $\eta_\perp = 100\ \mu\Omega$ m.

The code has reproduced the following key features observed in the experiments: (1) the RMF can produce steady-state current drive even though barely reaching the field null; (2) the $B_z(r)$ profile exhibits a distinctive flat region around the field null where little current drive is necessary, or available. In addition, the code predicts a steady inward flow of about 4 km/s across the field null, which is allowed for by stipulating a rate of swirling flow, driven by high pressures on the inner field lines. However, the computed magnetic field profiles appear to be much steeper in the regions just inside and outside the field null, compared to the experimental data shown in Fig. 16. One possible explanation is that the anomalous radial transport is stronger around the field null where the axial field strength is small, as would be im-

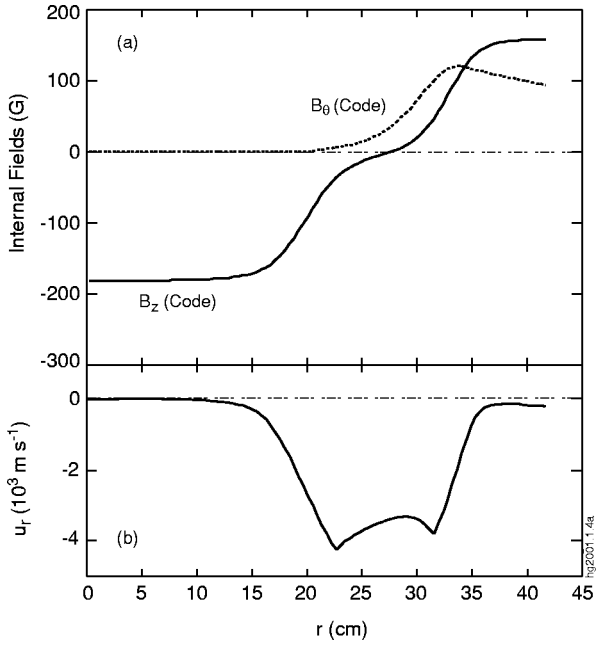

FIG. 18. Results from a 2D RMF current drive code: (a) axial magnetic field B_z and RMF B_θ; (b) radially inward flow, u_r, predicted by the code.

plied by Bohm transport (discussed in Sec. IV B). Some 3D effects due to limited RMF antennae length, particle recycling at the ends, etc., might also be responsible. Detailed comparison with experimental data using various model assumptions is a subject for future publication.

Figure 19 shows the on-axis ($r=0$) axial magnetic fields as a function of the distance from the midplane, measured by an internal magnetic probe inserted from the end of the TCS chamber (Fig. 1), together with the vacuum bias fields. In the figure are also shown the external magnetic fields measured by two external magnetic loops located at the midplane and the end region, outside the quartz vacuum vessel wall. We can see that the separatrix location z_s is well defined (central axial field B_z changes sign), and is away from the end cone, as indicated in the figure.

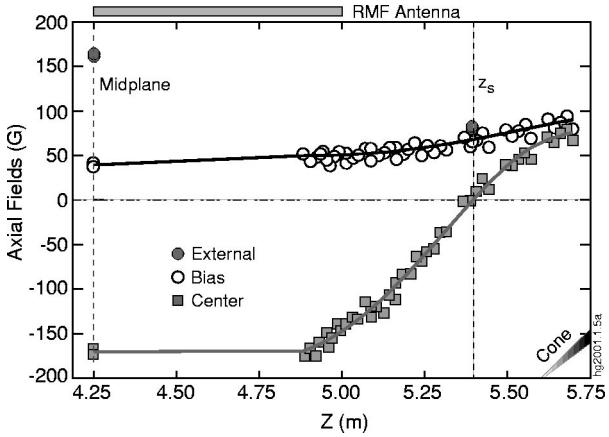

FIG. 19. Axial profile of the axial magnetic fields at $r=0$ (solid squares), and the external fields at two positions (solid circles), for a series of repeatable discharges. The initial axial bias field profile prior to the onset of a discharge (open circles) is also shown. The positions of the RMF antenna and the end cone are indicated.

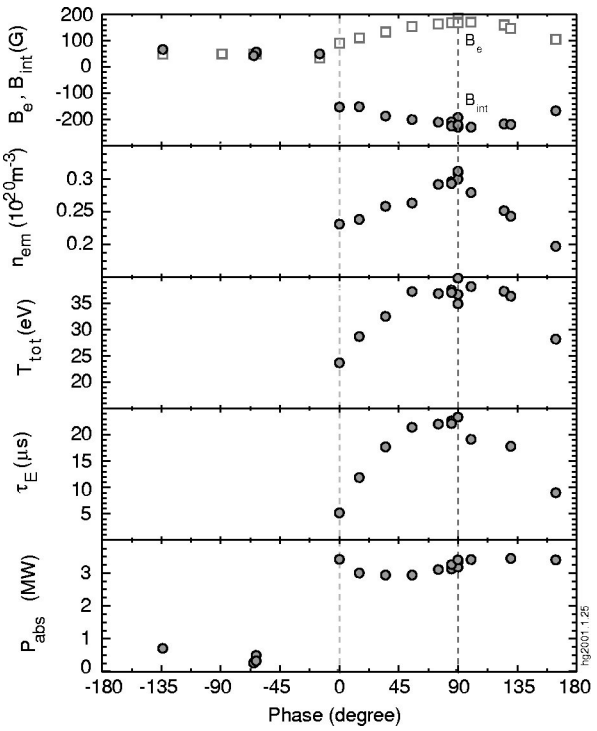

FIG. 20. Effect of phase shift between horizontal and vertical oscillating magnetic fields. The data shown are external (B_e) and internal (B_{int}) magnetic fields, peak plasma density (n_{em}) and total temperature (T_{tot}) derived from radial pressure balance, energy confinement time [$\tau_E = E_p/(P_{\text{abs}} - dE_p/dt)$], as well as the total input power (P_{abs}), for a series of identical discharges except that the phase was varied.

D. Dependence on phase shift between horizontal and vertical RMF fields

To generate and sustain the toroidal current in the FRCs, the RMF must rotate in the electron diamagnetic direction. This requires that the phase of the horizontal oscillating magnetic field be delayed by 90° with respect of the vertical magnetic field under the particular magnetic configuration for our RMF experiments. The effect of the phase delay between the horizontal and the vertical fields is illustrated in Fig. 20 where data was taken during the steady state phase of a series of otherwise identical discharges with the phase varied between 0 and 360 degrees. Best performance was achieved for a 90° phase separation, as expected, but the peak is fairly broad making precise phase control unnecessary. Some current is even produced for zero phase shift as recently demonstrated by Xu *et al.*[19] but many nonsimple effects could account for this. The power deposited to the plasma, P_{abs}, is also shown. There is little variation for the phase between 0° and 180°, but the absorption is greatly reduced for the RMF rotation in the wrong direction, presumably due to poor penetration. The derived energy confinement time is also shown, and displays the same peak near a phase separation of 90°.

E. Energy losses and particle confinement

The energy confinement time can be simply defined as $\tau_E = E_p/(P_{\text{abs}} - dE_p/dt)$. Measurements in previous, nonsustained, theta pinch formed FRCs involved some compressional input from the theta pinch coils, but were primarily dominated by dE_p/dt. In the present case dE_p/dt is small and the calculation is dominated by the RMF input power. This is difficult to ascertain since each of the two antennas (vertical and horizontal) is feeding a nearly inductive load. One cannot simply measure the difference in capacitor bank supply voltage decay between a vacuum and plasma shot since the presence of a plasma greatly changes the pulser tube currents, and hence the tube losses. The technique adopted was to carefully measure the antenna voltage and current traces and add a time delay so that they were exactly 90° out of phase for a vacuum shot. The integral of $I_{\text{ant}}V_{\text{ant}}$, when averaged over many cycles, then gave precisely the power input to the plasma from each antenna. Since typical antenna currents and voltages were $\sim\pm 10$ kA and ± 10 kV, it was important to determine the phases between I_{ant} and V_{ant} to within one-half a degree (17 ns for the 80 kHz frequency) to obtain accuracies of under 1 MW. This was less than the time interval for our 10 MHz digitizers but, using smoothing and the above-mentioned time shift techniques we generally achieved errors, as measured by examining many vacuum shots, of under 0.5 MW. More details can be found in Ref. 20.

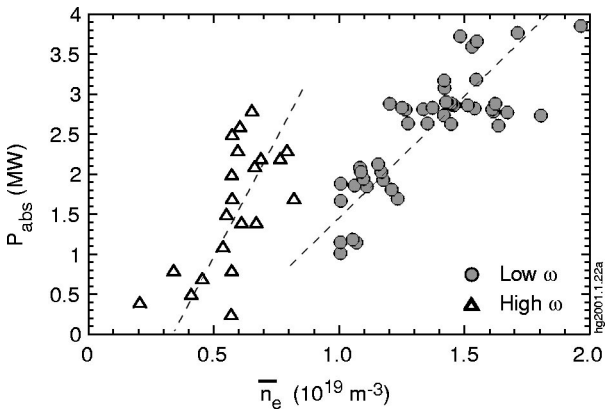

FIG. 21. RMF absorbed power P_{abs} deposited to the plasma as a function of the line averaged density $\langle n_e \rangle$ measured at the axial midplane.

Measured absorbed power, for both the $\omega = 10^6$ and $\omega = 0.5\times 10^6$ rad/s cases are shown on Fig. 21. The absorbed power per unit length

$$P'_{\text{abs}} = \eta_\perp \int 2\pi r j_\theta^2 \, dr \tag{17}$$

should scale as $\eta_\perp B_e^2/\Delta r$ or $\eta_\perp B_e^2/\zeta$ or $\eta_\perp \omega n_e B_e$. The absorbed power due to the axial screening currents will scale in the same manner, as $0.5\eta_\parallel (2B_\omega)^2/\Delta r$, and its contribution will depend on the relative value of $\eta_\parallel$ and $\eta_\perp$. (Actually $\eta_\parallel$ may be a misnomer since the electric field is in the z direction, while the axial field lines become helical due to the RMF B_θ.) The analytic scaling results do not depend on the ratio of $\eta_\parallel/\eta_\perp$, but if it is not small, then axial current dissipation could add to the absorbed power. Since both n_e and B_e are both observed to scale approximately linearly with B_ω, the observed linear scaling of P_{abs} with n_e implies that $\eta_\perp$ sales inversely with n_e, in agreement with the scaling data shown in Fig. 14. The reason the absorbed power is

higher for higher RMF frequency at a given density is that the current carrying region is thinner (reduced Δr) and the FRC is longer.

There are still some discrepancies between the Fig. 14 and Fig. 21 inferences about plasma resistivity. By integrating Eq. (17) over just the outer field lines, the absorbed power per unit length can be written as

$$P'_{\rm abs}=k_a\frac{2\pi r_s}{\Delta r}\eta_\perp\left(\frac{B_e}{\mu_0}\right)^2=k_a\frac{\pi}{\langle\beta\rangle\zeta}\eta_\perp\left(\frac{2B_e}{\mu_0}\right)^2, \tag{18}$$

where $\Delta r/r_s$ is related to ζ by Eq. (2). For a rigid rotor density and current profile over a current sheet width Δr the factor $k_a\approx 2$ due to current concentration at the higher density. The numerical calculations, even including the inner field line losses, yield a factor of $k_a=0.5$ due to a wider current carrying profile (Fig. 18). The experimentally measured profiles (Fig. 16) are wider still and can be represented by $k_a\approx 0.35$. Using the numerical value, the resistivity inferred from the absorbed power is about a factor of 2 higher for the $\omega=0.5\times 10^6$ data than inferred from the $\gamma/\lambda=1/\sqrt{2}$ scaling. This discrepancy could be due to experimental errors in determining the current profile, to axial current dissipation, or to the extreme simplification of the analytical model. However, one would expect the analytic scaling to be conservative since the RMF must drive current beyond the extent of the antennas.

In any case, the energy confinement times are typically only on the order of 30 μs. The values of flux confinement time given by the rigid rotor formula, $\tau_\phi=r_s^2/16D_\perp$, are on the order of 100 μs for the typical 100 m^2/s diffusivities (125 $\mu\Omega$ m resistivity). This value is also consistent with the observed flux decay rates after the RMF is shut off. Hopefully, the resistivity will decrease to the low values seen for the hotter, higher density translated FRCs in future experiments.

Since the absorbed power is so high, it is of interest to determine where it is going. Radiative power has been measured by a Bolometer viewing across the FRC midplane, and multiplying the result by the ratio of total FRC volume to viewing volume. These results are shown in Fig. 22 as a function of $n_e^2T_{\rm tot}$. $T_{\rm tot}$ is the total temperature inferred from the density and pressure balance, and is assumed to be almost completely electron temperature. For a given density the radiation power is higher for the higher frequency case, perhaps due to a more concentrated deposition volume and a higher level of impurities there.

Due to lack of detailed profile measurements of FRC density and (electron/ion) temperatures, we have developed a zero-dimensional (0D) model for global particle and power balance. For all the discharges presented in this paper, the time scale for changes in the global plasma parameters such as density, power, external fields, etc., during the quasisteady phase of the discharges, are much longer than the energy and flux confinement times. Therefore, the FRCs are simply treated as steady state in the following analysis. Conduction losses are neglected due to the low electron temperature and near vacuum separatrix pressure over most of the FRC, and the RMF heating power is assumed to be balanced by ionization (P_i), convection ($P_{\rm conv}$), charge exchange ($P_{\rm cx}$), and radiation ($P_{\rm rad}$).

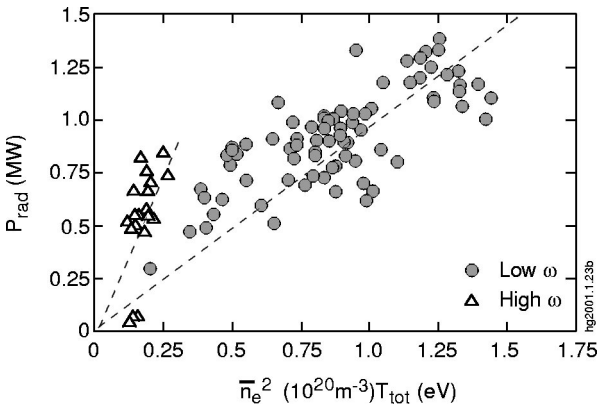

FIG. 22. Radiative power, $P_{\rm rad}$ versus $\langle n_e\rangle^2T_{\rm tot}$, with $T_{\rm tot}$ being the pressure balance temperature.

$$P_{\rm abs}=P_i+P_{\rm conv}+P_{\rm cx}+P_{\rm rad}. \tag{19}$$

Particle loss through the convection channel should be balanced by the rate of ionization since the total particle inventory is also quasisteady and recombination is only important when the electron temperature is below 1 eV. Thus, we obtain

$$P_{\rm abs}=n_en_nS_iV_0(\varepsilon_i+2.5kT_{\rm tot})+n_in_nS_{\rm cx}V_02.5kT_i+P_{\rm rad}. \tag{20}$$

n_n is the neutral density which exists only in the volume $V_0=(1-(1-\lambda_0/r_s)^2)V_{\rm FRC}$ where λ_0 is the mean free path of neutrals before ionization. S_i and $S_{\rm cx}$ are the rate coefficients for ionization and charge exchange, respectively, and ε_i is the ionization energy (13.6 eV per ionization). The neutral density, n_n, is not measured and is specified as a free parameter. In addition, though the total temperature $T_{\rm tot}$ is derived from radial pressure balance, no entirely accurate measurements of either T_e or T_i are presently available. In the calculation, two cases are considered: (1) $T_i=0$ and (2) $T_i=T_e$. Power losses in each separate channel can then be identified.

As an example, Fig. 23 shows the calculated power losses for a reduced ω discharge, assuming $T_i=T_e$, along with the measured RMF heating power and the radiative power. In order to match the input RMF heating power, a neutral density $n_n=0.06n_e$ has to be assumed in Eq. (20). Table I lists the power losses in each channel, together with the values for the neutral concentrations required to achieve power balance at 800 μs of the discharge (pulse 3179), for both the $T_i=0$ and the $T_i=T_e$ cases.

The global particle confinement time can be defined as

$$\tau_N=\frac{N}{\Gamma_{in}-dN/dt}, \tag{21}$$

where N is total number of particles in the confined plasma volume, and $\Gamma_{in}=n_en_nS_iV_0$ is the particle influx. For the steady state FRCs, Eq. (21) can be simply rewritten as

$$\tau_N=1/(n_nS_if_V), \tag{22}$$

where $f_V=V_0/V_{\rm FRC}$ is the fraction of FRC containing neutrals. Since the RMF drives plasma inward and produces a

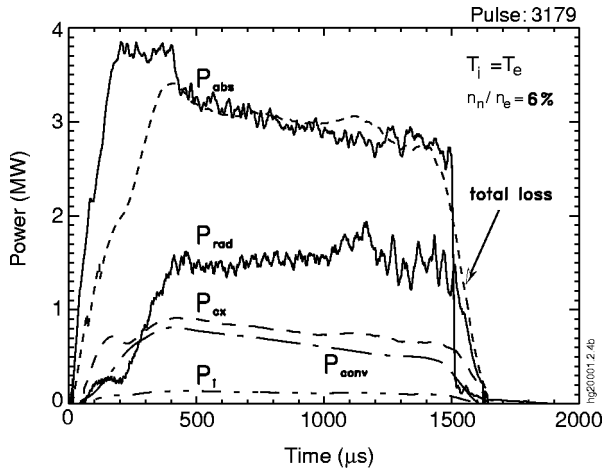

FIG. 23. Power loss in different channels for a discharge with $\omega = 0.5 \times 10^6$ rad/s, $B_\omega = 75$ G, and $\langle n_e \rangle \approx 2 \times 10^{19}$ m^{-3}, including convection, ionization, and radiation derived from global power balance for a particular case assuming $T_i = T_e$. The total RMF input power is also shown.

very low separatrix density, the particle loss balancing ionization presumably comes from the FRC ends, or radially from the portion outside the RMF antennas. The observed time independence of N could be self-regulating due to the FRC expanding past the RMF antennas until the outflow just balanced the ionization derived inflow.

The calculated values of τ_N for both the low RMF frequency and the high RMF frequency discharges are shown in Fig. 24 based on $T_i = T_e$. (Assuming $T_i = 0$ leads to somewhat lower confinement times due to a reduction in charge exchange losses.) It is interesting to note that the particle confinement time in these low temperature RMF formed FRCs exhibits a similar size scaling, i.e., $\tau_N \propto x_s r_s^2$, to that seen in conventional hot FRCs, albeit at a lower absolute value.[8]

F. Effect of neutrals on ion spin up

In the presence of the RMF, the ions are subject to a frictional drag force applied by the electrons, given by

$$f_{su} = \nu_\perp m_e (\omega - \omega_i) r \tag{23}$$

assuming that electrons rotate synchronously with the RMF and the ions have a rotational frequency ω_i. The ion spin-up time is simply

$$\tau_{su} = m_i \omega r / f_{su} = (m_i / m_e) \nu_\perp^{-1}. \tag{24}$$

It would take only ~ 100 μs for ω_i to reach ω for the present RMF formed FRCs due to the elevated resistivity ($\eta_\perp = m_e \nu_\perp / n_e e^2 \sim 100$ $\mu\Omega$ m and $\nu_\perp \sim 50 \times 10^6$ s^{-1}). This is, however, not observed in the experiments.

TABLE I. Inferred powers for the shot shown in Fig. 23 at 800 μs.

	P_{abs} (MW)	P_{rad} (MW)	P_i (MW)	P_{conv} (MW)	P_{cx} (MW)	n_n / n_e
$T_i = 0$	3.12	1.4	0.26	1.5	0	0.13
$T_i = T_e$	3.12	1.4	0.15	0.7	0.8	0.06

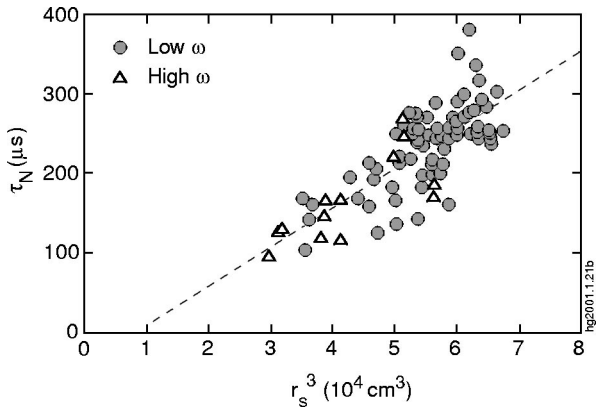

FIG. 24. Particle confinement time, τ_N versus r_s^3 based on inferred ionization rate, for the $T_i = T_e$ case.

It has been proposed that cold neutrals provide this slowing down action by transferring momentum with the ions.[9,10] Assuming a retarding force $f_{in} = \nu_{in} m_i \omega_i$ due to stationary neutrals, the resultant ion rotational speed fraction is

$$\alpha = \frac{\omega_i}{\omega} = \left(1 + \frac{m_i}{m_e} \frac{\nu_{in}}{\nu_\perp} \right)^{-1}. \tag{25}$$

The ion-neutral momentum transfer collision frequency can be represented by charge exchange, $\nu_{in} = S_{cx} n_n$, where n_n is the neutral density, and S_{cx} is the rate coefficient for charge exchange.[21]

The experimental data, obtained from multichannel Doppler spectroscopy, are shown in Fig. 25(a) for the discharges conducted with the RMF operated at both $\omega = 0.5 \times 10^6$ and 10^6 rad/s. In Fig. 25(b) are shown the corresponding neutral concentrations (solid symbols), derived from global power balance. It can be seen that the spin-up parameter α of the C^{++} ions rises as density increases and, indeed, correlates with a decrease in neutral concentration.

The number of neutrals required to slow down the ions can be estimated using Eq. (25). The calculated result is also shown in Fig. 25(b) by the open symbols, assuming $T_i = T_e$. This neutral fraction shows a similar decreasing trend with density as inferred from power balance, but with a much higher magnitude, especially for the higher ω, low density discharges. Measurement of neutral densities is obviously a high priority for RMF operation.

Note that in conventional theta pinch formed FRCs it has been observed that ions tend to rotate in the ion diamagnetic direction, i.e., opposite to the RMF rotational direction. The mechanisms responsible for this, such as particle loss or end-shorting,[17] may also be active in the RMF formed FRCs, thus offsetting the ion spin-up rate by the applied RMF.

As can be seen in Fig. 25(a), the ion spin-up frequency is higher in the reduced ω discharges than for the higher ω experiments, despite the lower drive frequency. This usually results in development of the standard $n = 2$ rotational instability, while $n = 1$ modes have been the predominant instabilities present in the previous high ω discharges. The $n = 2$ modes tend to develop in the discharges with a low density, resulting in a small FRC with short axial length and small separatrix radius. This is illustrated in Fig. 26, where other-

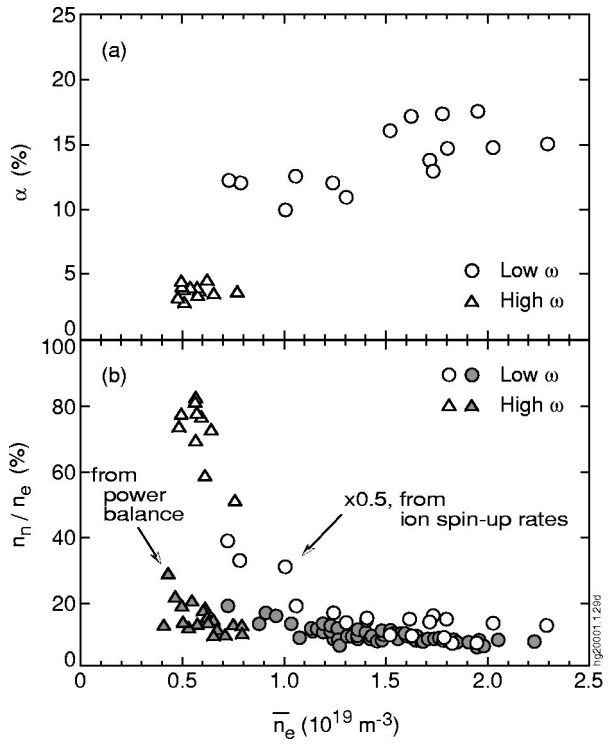

FIG. 25. (a) Ratio of the rotation speed of C^{++} ions, determined from Doppler shift of CIII line at 464.7 nm, to the RMF rotation velocity, $\alpha = \omega_i / \omega$, and (b) calculated fraction of neutrals, n_n / n_e, based on power balance (solid symbols), together with the values calculated using Eq. (25) (open symbols) with an assumption of $T_i = T_e$.

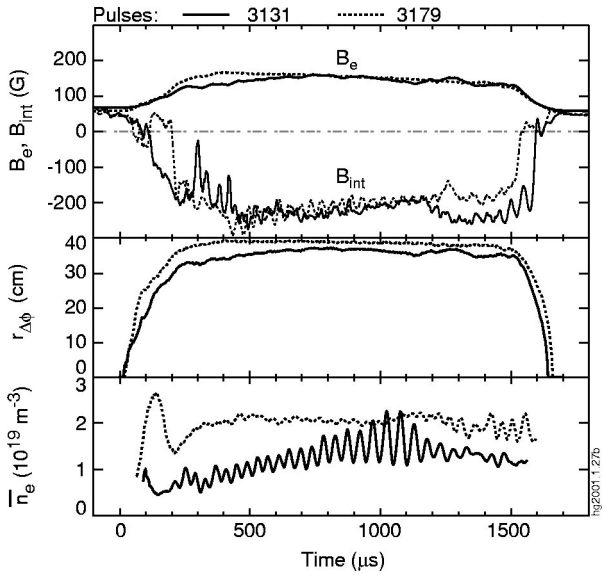

FIG. 26. Evolution of two comparable discharges with different densities. The data shown are the internal (B_{int}) and external (B_e) magnetic fields, the excluded flux radius ($r_{\Delta\phi}$), and the plasma line averaged density ($\langle n_e \rangle$).

wise identical discharges, with different puff–fill pressures are shown. It is interesting to note that similar performance is achieved in the lower density case despite the strong $n=2$ oscillations. Operation at stronger bias fields compresses the FRCs further away from the wall, making them more prone to the rotational instabilities. As in the high ω discharges, the rotational modes rotate in the RMF direction with a frequency in the range of tens of kHz, similar to the ion rotational frequency.

V. SUMMARY AND IMPLICATIONS

FRCs have been sustained in quasi-steady-state for the first time inside a standard flux conserver. Up to 60 kA of toroidal current has been driven by rotating magnetic fields. These RMF driven FRCs behave in accordance with the simple analytic scaling laws developed in Ref. 7 and further expanded upon by the numerical calculations of Ref. 11. The important parameter governing performance is the cross-field resistivity, which is very high ($\sim 100\ \mu\Omega\,\mathrm{m}$) for the present low temperature, solely RMF formed FRCs. It is probably not possible to reach higher temperatures in any high beta plasma by slow formation techniques due to radiation barriers at the initial high densities and high-, low-temperature loss rates. Higher temperature RMF drive experiments will have to wait upon more standard FRC formation methods.

In accordance with theory, RMF drive causes FRCs to expand and increase in density until the frictional torque due to electron–ion resistivity equals the RMF imposed torque. If the initial bias field inside the flux conserver is chosen in the correct range for the expected resistivity, the FRC separatrix radius will expand to large values of $x_s \equiv r_s / r_c$ since it is this radial expansion inside a flux conserver that provides for higher axial confinement fields and higher plasma density. When equilibrium torque balance is reached the RMF will never penetrate much beyond the axial field null as long as the parameter ζ, equal to the line current needed to reverse the external field divided by the full possible synchronous current, is less than unity. Best drive efficiency is achieved when ζ is close to unity, and RMF frequencies should be chosen accordingly. Low ζ and the resultant edge current drive produces pressure profiles inconsistent with FRC axial equilibrium constraints, and leads to unsteady behavior that must surely affect confinement. Higher external fields, and more energetic FRCs could be sustained, even with the present high resistivities, if the FRC temperature increased, but this has not been possible with moderate power RMF formation alone.

For the present experiments, better performance has been achieved by lowering the RMF frequency to increase ζ. This allowed higher RMF fields to be produced, resulting in higher densities and external fields, but brought ζ back below 0.3. One consequence of reducing the RMF frequency and increasing its strength was that $\omega_{ci} = eB_\omega / m_i$ became comparable to the RMF frequency ($\omega_{ci}/\omega = 0.65$ for $B_\omega = 70$ G). It had been postulated by early developers of fully penetrated RMF drive theory that it was necessary to have $\omega_{ci} \ll \omega$ to avoid also driving a synchronous ion current, but Hoffman[22] showed, using particle orbit calculations, that the ions may only achieve rotational speeds equal to $(B_\omega / 2B_z)\omega_{ci}$. In any case, the physics is very different for the partially penetrated RMF that will always occur in flux confined FRCs with $\zeta < 1$. No particular problems were encountered with $\omega_{ci}/\omega = 0.65$.

As predicted by many researchers, the ions should spin-up in the RMF direction due to electron–ion friction. This appears inevitable since the RMF applies an actual torque to the plasma. Either a source of new particles (fueling) or the presence of a neutral background can absorb this torque and lead to a reduced ion rotational speed. Inferences of neutral density from energy confinement times in the present experiments yield neutral fractions in the correct range to limit the ion rotational velocities to observed values. Most likely coincidently, these speeds are also roughly in agreement with those predicted from the particle orbit calculations.

Even with partial spin-up the ions are rotating at speeds equal to or greater than their thermal velocities. It is thus not surprising that plasma spin-up is always accompanied by some degree of rotational distortion. At low velocities the distortion is mostly $n=1$ (a wobble) as has been noted in many theta pinch devices, and is generally nondestructive. At higher velocities the $n=2$ distortion is dominant, but also does not result in destruction of the large x_s plasmas.

A basic component of the simple theory is that an inward flow (possibly only of electrons) is required to maintain current on the inner field lines. The conjecture of a total plasma inward v_r is supported by the measured higher pressure on the inner flux surfaces. It is not known if this inward flow is sustained by the swirling flow assumed in the numerical calculations,[11] or simply by inflow and ionization of a neutral background. At the lower densities produced by the high ω drive, the ability to sustain the FRCs for long times was dependent on the end treatment. In the STX experiments at similar sub 10^{19} m^{-3} densities it was never possible to maintain the FRC flux for the duration of the RMF.[5] This may signify that a significant part of RMF current drive involves a supply of fueling particles at the edge. It would also account for the discrepancy noted between Figs. 14 and 21 where the $\gamma/\lambda = 1/\sqrt{2}$ scaling yields large resistivities at low density, but the absorbed power appears to be low. The lack of an adequate particle supply could be what is limiting low density performance, rather than the high resistivity predicted by the γ/λ scaling. The exact mechanism, whether edge fueling or swirling flow, has implications for future experiments with better particle confinement and hopefully lower neutral backgrounds.

In any case, at higher densities there will eventually be a need to counter the RMF torque by some means other than a neutral background. Neutral beam injection in the anti- RMF direction can supply this momentum source, and also contribute to current drive. RMF drive has demonstrated the ability to counter radial particle diffusion and, in concert with edge NB fueling, could have the additional benefit of reducing conduction losses, especially if the ratio B_ω (and especially B_r) to B_z is small. This may be the ideal FRC sustainment technology, relieving some of the requirements on RMF power, whatever the actual plasma resistivity. However, the next step is to demonstrate RMF current drive in hot, lower resistivity FRCs. This program is currently underway in the TCS theta pinch formed and translated FRC program.

ACKNOWLEDGMENTS

It is a pleasure to acknowledge the contributions from the rest of the RPPL staff. In particular, the authors gratefully acknowledge E.A. Crawford, R.D. Milroy, J.T. Slough, and L.C. Steinhauer for fruitful discussions, and J. Hayward, S. Kimball, M. Kostora, and D. Lotz for technical support.

This work was supported by USDOE Grant No. DE-FG03-96ER54376.

[1] N. Donaldson, R. Hahnheuser, I. R. Jones, G. Staines, and S. Xu, Plasma Phys. Controlled Fusion **36**, 259 (1994).
[2] N. Donaldson, P. Euripides, I. R. Jones, and S. Xu, Plasma Phys. Controlled Fusion **37**, 209 (1995).
[3] P. Euripides, I. Jones, and C. Deng, Nucl. Fusion **37**, 1505 (1997).
[4] A. L. Hoffman, H. Y. Guo, J. T. Slough, S. J. Tobin, L. S. Schrank, W. A. Reass, and G. A. Wurden, "The TCS rotating magnetic field current drive experiment," to be published in Fusion Technol.
[5] J. T. Slough and K. E. Miller, Phys. Plasmas **7**, 1945 (2000).
[6] J. T. Slough and K. E. Miller, Phys. Rev. Lett. **45**, 1444 (2000).
[7] A. L. Hoffman, Nucl. Fusion **40**, 1523 (2000).
[8] A. L. Hoffman and J. T. Slough, Nucl. Fusion **33**, 27 (1993).
[9] W. N. Hugrass, J. Plasma Phys. **28**, 369 (1982).
[10] M. Ohnishi and A. Ishida, Nucl. Fusion **36**, 232 (1996).
[11] R. D. Milroy, Phys. Plasmas **7**, 4135 (2000).
[12] I. E. Jones and W. N. Hugrass, J. Plasma Phys. **26**, 441 (1981).
[13] W. N. Hugrass and R. C. Grimm, J. Plasma Phys. **26**, 455 (1981).
[14] R. D. Milroy, Phys. Plasmas **6**, 2771 (1999).
[15] K. Suzuki and S. Hamada, J. Phys. Soc. Jpn. **53**, 16 (1984).
[16] A. M. Peter (private communication).
[17] M. Tuszewski, Nucl. Fusion **28**, 2033 (1988).
[18] W. T. Armstrong, R. K. Linford, J. Lipson, D. A. Platts, and E. G. Sherwood, Phys. Fluids **24**, 2068 (1981).
[19] S. Xu, W. Luo, K. N. Ostrikov, J. Ahn, and S. Lee, Plasma Phys. Controlled Fusion **42**, 807 (2000).
[20] S. T. Tobin, W. A. Reass, L. S. Schrank, G. A. Wurden, H. Y. Guo, A. L. Hoffman, and D. Lotz, Rev. Sci. Instrum. **72**, 3528 (2001).
[21] M. F. A. Harrison, "Atomic and molecular collisions in the plasma boundary," in *Physics of Plasma-Wall Interactions in Controlled Fusion*, edited by D. E. Post and R. Behrisch (Plenum, New York, 1986), p. 281.
[22] A. L. Hoffman, Phys. Plasmas **5**, 979 (1998).